EFFICIENT NUMERICAL ANALYSIS OF DIRECTED ENERGY DEPOSITION PROCESSES

B. A. M. ELSNER*, I. NEUBAUER**, L. RABERGER***

*Simufact Engineering GmbH, 21079 Hamburg, Germany, Orcid Id: **0000-0003-4244-1886**
**Simufact Engineering GmbH, 21079 Hamburg, Germany
***Fronius International GmbH, 4600 Thalheim bei Wels, Austria

DOI 10.3217/978-3-85125-968-1-27

ABSTRACT

Directed energy deposition (DED) presents a versatile method in the field of Additive Manufacturing that allows to create complex structures by continuously welding new filler material to the underlying structure. The technology is developing quickly and DED structures with several kilometres of weld length are already engineering reality. Although numerical analysis has proven a valuable tool for the evaluation and understanding of different welding processes, typical transient simulations cannot handle such long weld tracks as time needs to be discretized in increments short enough to track the movement of the weld source in steps not larger than its own dimension. In this contribution, we present an Advanced Thermal Cycle (ATC) that allows to reduce the number of computational steps while still capturing the heat source's movement, local temperature differences, and maintaining the correct energy balance. The approach is validated by comparing the simulated thermal profile with the thermal history measured both for the substrate and the deposited weld filler of a demonstrator part.

Keywords: additive manufacturing, directed energy deposition, welding simulation, finite element method, thermal history

INTRODUCTION

Directed energy deposition (DED) refers to a family of Additive Manufacturing (AM) methods in which a metal filler material is continuously molten by a focused energy source and deposited onto the underlying substrate to create new features or entire components [1]. Filler materials include powder or wire feedstock, while energy sources may encompass virtually all welding technologies ranging from laser or electron beam to arc and plasma welding. In contrast to powder bed fusion (PBF) processes, DED is not limited to a single build direction or the restricting dimensions of a build tank while offering much higher deposition rates. Due to this vast potential, DED technology is evolving rapidly, and successful builds of sophisticated large-scale components have already been reported [2], [3], [4].

Despite these successes, DED still holds many challenges related to the complex thermal history that the deposited material experiences during many subsequent heating

and cooling cycles. As local characteristics of the final part – such as microstructure, phase transformations, or residual stresses – strongly depend on local temperature gradients [5], a thorough understanding of the DED part's thermal history is crucial for an optimized choice of process parameters and tool path planning. Numerical process simulation offers the unique opportunity to evaluate the thermal history of a DED build without the need for elaborate experimental set-ups or the use of expensive machinery, material, or operating staff. It gives access to results which are difficult to measure during the real process and allows to compare different process variants before the first real component is manufactured.

Transient, thermo-mechanical computational weld mechanics (CWM) approaches have already been demonstrated to be capable of capturing both the local thermal history as well as the distortions arising during the DED process [6], [7]. Such models offer a detailed representation of the weld source movement and its heat input into the deposited material and are thus well-suited to evaluate local temperature gradients with a high resolution. However, the computational cost of such DED simulations strongly depends on the applied discretization in space and time and therefore increases dramatically with the total length of the deposited weld bead. This issue is illustrated by the sample component presented in [6]. In this case, the transient, thermo-mechanical simulation required 100.9 h for depositing the 17.4 m of weld bead while the real build time only amounted to 74 min.

The spatial discretization is determined by the number of elements and nodes required to adequately mesh the DED deposit. In order to retain a detailed representation of material deposition, the element size ideally does not exceed the thickness of a single layer of deposited filler material. Thus, a longer weld bead quickly leads to a dramatic increase of the element count within the model. The issue of spatial resolution can be addressed via specific meshing techniques such as the mesh zoning approach presented in [8]. However, this topic will not be treated by the present contribution.

This contribution focuses on the discretization of process time. The models presented in [6] and [7] rely on a detailed time-stepping scheme that moves the weld source along the weld path in small time increments that are chosen such that there is a certain degree of overlap between the individual positions of the weld source. With weld source dimensions in the order of millimetres and total weld bead length in the order of metres to kilometres, the number of required time steps clearly becomes a limiting factor to the accessible model size. Similar restrictions apply to the simulation of PBF processes for which voxel approaches are applied to combine the heating of several powder layers into only a few computational increments [9]. Similar approaches have been followed in the context of DED by selectively heating entire layers [10] or pre-selected model sections [11]. While these approaches allow a significant speed-up of the simulation, they require the manual partitioning of the model into meaningful sections for heat input. The issue of manual model preparation is avoided by the elongated heat source model proposed in [12]. This approach performed well on the presented model of a simple wall, but its applicability may be limited for curved features that cannot be resolved by an elongated straight heat source.

This contribution presents the approach of an Advanced Thermal Cycle (ATC) that allows a simplification of the process by combining the heat input of an arbitrary number of smaller time steps whilst maintaining locally resolved the physical energy balance of

the process, similar to the technique proposed for powder bed fusion (PBF) in [13]. In the following sections, the model is introduced and for increasing simplifications of the model the quality of the resulting temperature distribution is benchmarked against an experimental reference.

METHODS

EXPERIMENTAL PROCEDURE

A thick-walled part was manufactured from G3Si1 wire filler material onto a S235JR steel substrate with the dimensions of 200 mm x 140 mm x 24 mm (length x width x height) using the Fronius CMT (Cold Metal Transfer) process.

The sample geometry consists of three subparts, as can be seen in Fig. 1(a). Subparts A and B are composed of 15 layers whilst subpart C only contains 14 layers; in total, 44 layers have been applied to form the part. Subpart C is missing one layer, due to an error in the tool path creation process.

The part was modelled in a CAD software and processed in the CAM software Mastercam (for slicing and tool path generation). It was then imported into Robotmaster; a software for robot-offline programming. The tool path for the first layer was applied to the substrate by the CMT-Marking process - as seen in Fig. 1(b). This allows visualization of the weld path before producing the part.

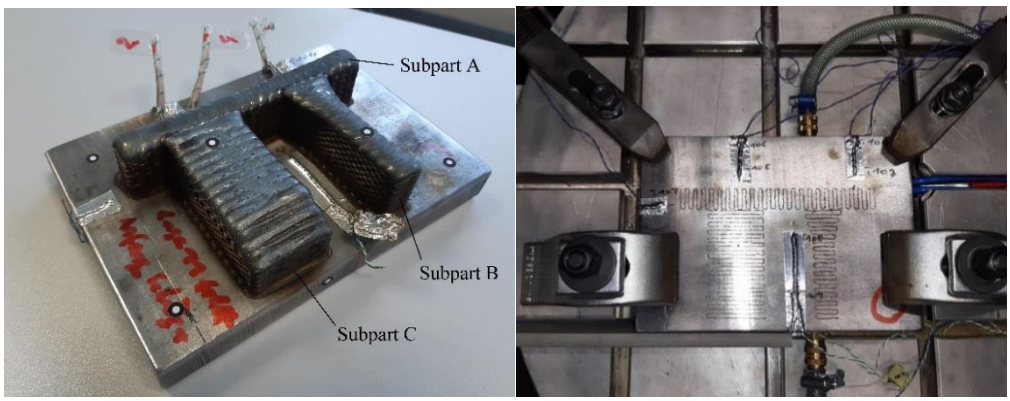

Fig. 1 (a) Welded part after cleaning. (b) Clamped substrate with weld path applied by CMT-Marking process and temperature sensors

The substrate was clamped on four different spots onto the horizontal table with a cooling plate positioned in between, as can be seen in Fig. 2(a). The cooling plate was designed such that the coolant, which flowed at a volume flow rate of approximately 6 l/min, could directly conduct the heat from the substrate. The design of the cooling plate can be seen in Fig. 2(b).

The part was produced using a Fronius TPS 600i PULSE in combination with a Fronius MTB 500i torch and ABB IRB 2600 robot. Shielding gas with a composition of 90% Argon and 10% CO_2 was used with a volume flow rate of 20 l/min.

Fig. 2 (a) Clamped welded part (b) Cooling plate

The mean temperature of the environment was 26.1°C. The feed flow and return flow temperature of the coolant has been measured and can be seen in Fig. 3. The feed flow temperature was relatively constant over time, whereas the return flow temperature fluctuates – highlighting the influence of the individual weld seams.

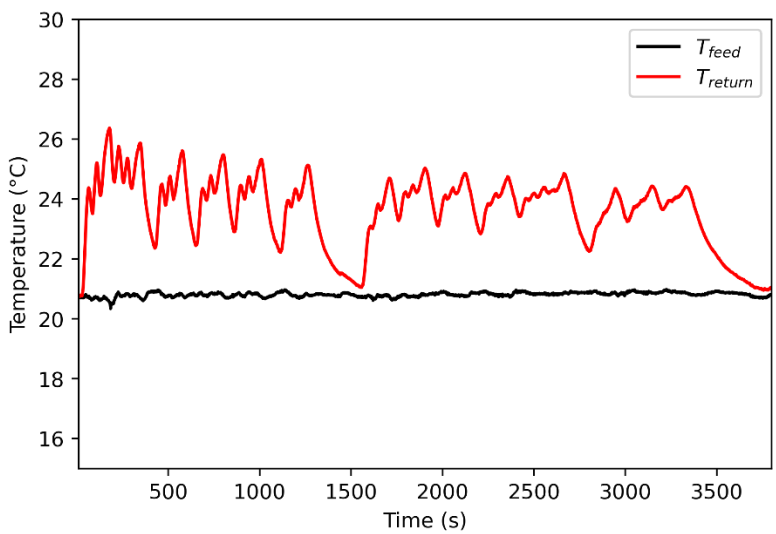

Fig. 3 Feed and return flow temperature of the coolant

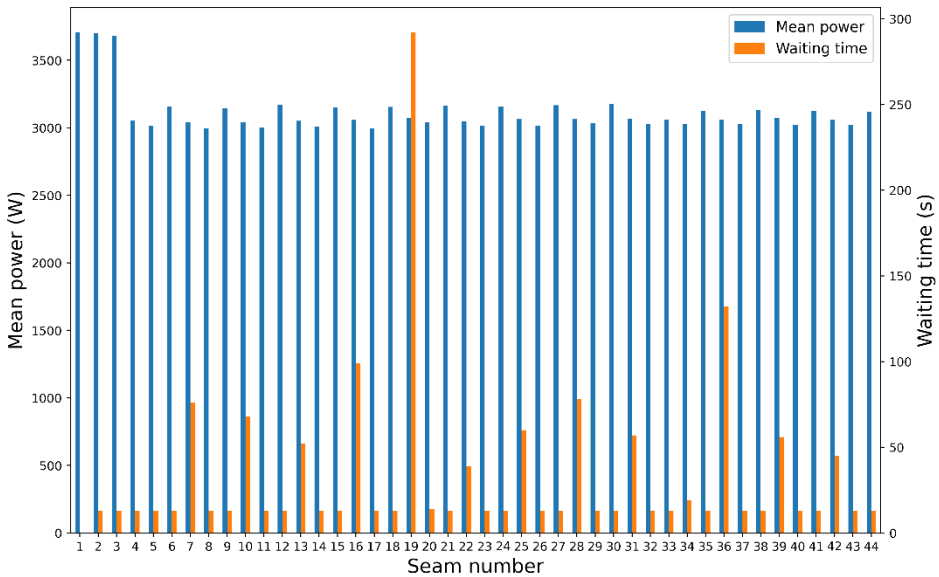

Fig. 4 Mean power per weld seam and waiting time before each weld seam

The mean values of power for each weld seam and the waiting times before each weld seam are displayed in Fig. 4. It should be noted that the set values of power for each weld seam were chosen from experience. Such that, the power was increased for the first layer to ensure sufficient bonding to the substrate and reduced to a relatively constant mean value for weld seams 4-44 (layers 2 to 14 respectively 15).

Temperature data was gathered by application of Type K thermocouples with a diameter of 0.2 mm to the substrate on seven different positions (Fig. 8). After application, the thermocouples were covered by aluminium foil tape. Additionally, Type K thermocouples with a diameter of 1.3 mm were applied manually into the weld pool during the welding process. However, useable data was only collected from three of these thermocouples, as the others were damaged by the arc during application. Due to this manual work the waiting times before each layer deposition varied as can be seen in Fig. 4.

The total build time, including waiting times between the seams as well as the time for cooling to room temperature at the end, was about 3800 s. The total welded filler material is 1.5 kg.

SIMULATION MODEL

All of the here-presented simulations are performed within the framework of the finite element (FE) model provided by the commercial welding simulation software Simufact Welding 2021.1. A fully transient, thermal DED simulation is set up as reference for the

simplifications introduced via the proposed Advanced Thermal Cycle (ATC) approach and to validate the model against the experimental measurements.

Fig. 5 illustrates the DED model. The deposit geometry is represented by 28352 eight-noded, isoparametric, three-dimensional hexahedral elements with trilinear interpolation which are defined to match the layer thickness of 2 mm. It is positioned on top of the baseplate which is cooled from below by the cooling system acting as a temperature sink at 22.2°C representing the mean temperature of the coolant (see Fig. 3). Heat loss to the 26.1°C environment is considered with a constant convective heat transfer coefficient of 20 W/(m²K) and constant emission coefficient of 0.6.

Both the baseplate and deposit are approximated with the same S235 material data from the Simufact Welding database. A linear decrease of density is assumed between 20°C and 1300°C. The relevant thermal properties are shown in Table 1 as well as in Fig. 6. The weld source is modelled as a double-ellipsoidal Goldak source defined by the constant parameters listed in Table 2. For each weld seam, the experimentally recorded mean power is applied as illustrated in Fig. 4. A tolerance of 20 K is set for thermal convergence.

The deposition of material during the DED process is controlled by the element-birth routine described in [6] which controls activation and heating of elements touched by the moving weld source. In order to fully capture the transient movement of the weld source, a fixed time increment of 84 ms is chosen, resulting in a total of 21628 increments calculated for welding. The total simulation, including additional 421 increments for cooling cycles, required a total computational time of about 44 hours on a 64GB RAM Windows machine with Intel® Xeon® W-2145 CPU @ 3.70 GHz processor.

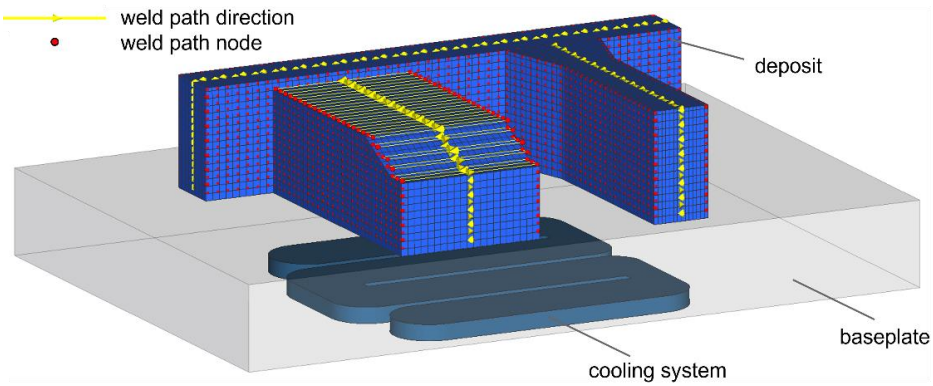

Fig. 5 Model set up in Simufact Welding

Table 1 S235 material data used for the DED simulations

Density (20°C)	Density (1300°C)	Solidus	Liquidus	Latent heat for melting
7852.2 kg/m³	7397.4kg/m³	1466.9°C	1517.1°C	256400.0 J/kg

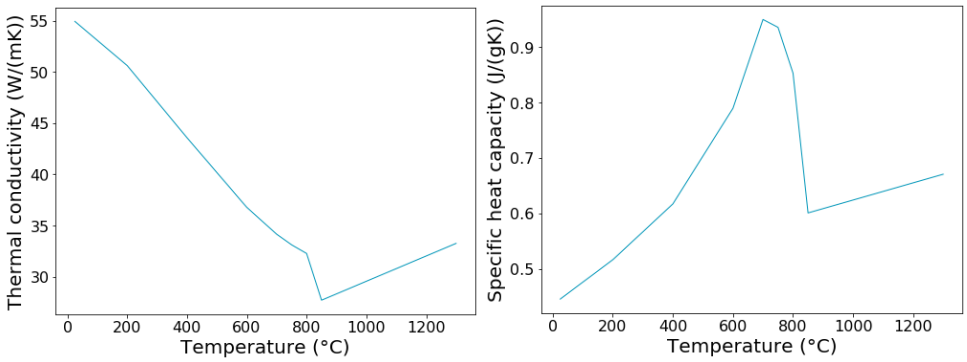

Fig. 6 Temperature-dependent thermal conductivity and specific heat capacity used for the DED simulations

Table 2 Layer-independent welding parameters

Velocity	Front length	Rear length	Width	Depth	Efficiency
20.0 mm/s	2.0 mm	4.0 mm	1.5 mm	3.5 mm	0.8

This fully transient model was simplified via an Advanced Thermal Cycle (ATC) that was implemented into the SF Marc solver utilized by Simufact Welding. Instead of calculating individual increments for all time steps, the ATC allows to combine an arbitrary number of time steps into segments which will then be treated in a combined fashion. The ATC is controlled by two parameters: the ATC-factor N and the ATC time step Θ.

The combination of time steps is controlled by the ATC-factor N which defines how many time steps are grouped together. With n being the total number of time steps required for transient treatment of a given weld bead, meaningful values for the ATC-factor encompass integer values in the range 2 to n. Accordingly, the total number of segments defined by the ATC-factor is the integer value of n/N.

For each segment, the solver internally processes N virtual time steps in which the weld source is moved along the weld path and the resulting fluxes are collected without applying them to the model yet. Once these virtual time steps are completed, two increments are calculated: In the first one, the accumulated heat fluxes are applied during the ATC time step Θ. With θ being the time the weld source requires to travel the complete segment, the duration of the second computed increment is set to $\theta - \Theta$. During this second increment, no heat fluxes are applied, and the segment is allowed to cool. Once both increments are completed, the next segment is considered in a similar fashion. In Fig. 7, this procedure is schematically shown for a weld path that requires 50 increments to complete in a transient analysis. In each of these increments, a constant heat flux of relative magnitude 1 is applied. Given an ATC factor $N = 10$ and ATC time step Θ

$= 2\ s$, the total number of increments required for welding reduces to 10 and the relative heat flux f_{rel} in every second increment is computed from $f_{rel} = \frac{\theta}{\Theta}$, thus increased to 1.25. Note that the total amount of heat entering the model per segment is identical for both the transient and ATC variants.

The ATC time step Θ is a free parameter that needs to be adjusted to calibrate the peak temperature reached in the model. If the value of Θ is increased, the peak temperature decreases as a greater amount of heat can be lost to the environment or conducted into the surrounding material during heating. Likewise, the peak temperature increases as the value of Θ decreased. There are two major advantages of this simplified approach: Unlike conventional thermal cycle approaches [14], [15], the ATC maintains the physical energy balance, globally and locally. At the same time, the total number of computed increments is reduced by the factor $2/N$, resulting in a considerable potential to reduce the required computational time.

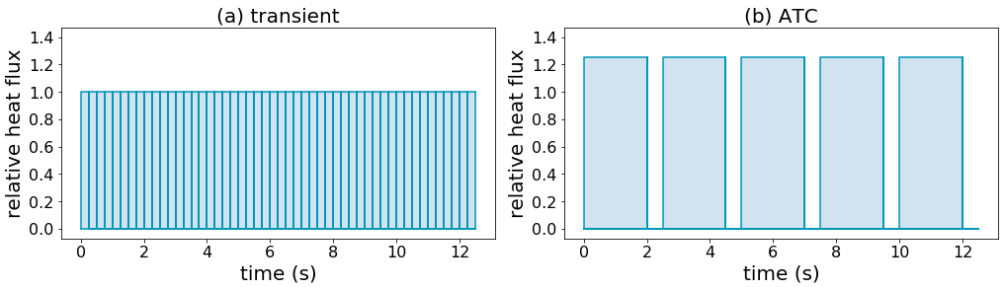

Fig. 7 Schematic illustration of the relative heat flux during a transient analysis with 50 increments and its simplification with ATC factor $N = 10$ and ATC time step $\Theta = 2\ s$. The time required to complete each segment is $\theta = 2.5s$.

RESULTS AND DISCUSSION

VALIDATION OF THE REFERENCE MODEL

In order to validate the transient reference model, temperatures were recorded for 10 positions on the baseplate and deposit as shown in Fig. 8. Although the model was set up according to the experimental process parameters, a slight timing offset was found between the experimental and numerical data sets increasing towards the end of the process. This effect is attributed to limited precision in the available velocity data of the welding robot which adds up to the observed offset of temperature peaks. To ease comparison between experimental and numerical data, the numerical time is scaled with a factor of 1.01. With this correction, Fig. 9 highlights the good agreement between numerical and experimentally measured temperature data.

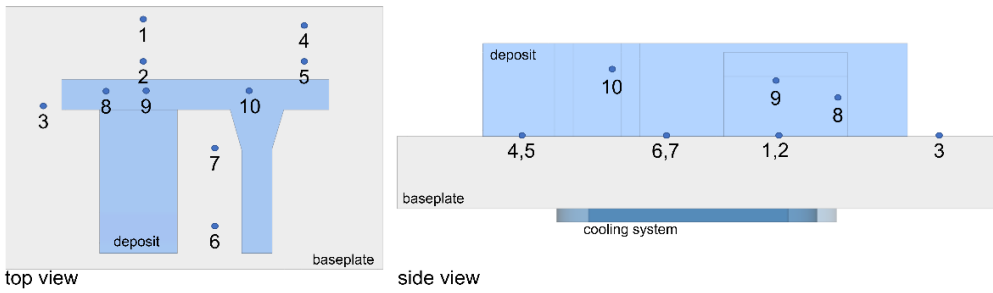

Fig. 8 Positions of temperature measurement

Temperature differences between numerical and experimental data are shown in Fig. 10, with the corresponding values for mean and standard deviation listed in Table 3. The best agreement between numerical results and experimental data is found at measurement positions 1 and 4, situated on the baseplate at some distance to the deposit. In these positions, the mean and the standard deviation of the temperature difference are smaller than 10 °C, indicating excellent agreement between model and reality. Positions 2, 3, and 5 are also located on the baseplate, but closer to the deposit. In these positions, the mean temperature difference is still below 10 °C, but with slightly increased standard deviations up to 23 °C. Also positions 6 and 7 are located on the baseplate, enclosed by the deposit in three directions. Contrary to points 1 to 5, in these positions, the numerical prediction slightly underestimates the measured temperatures, highlighted by the mean temperature difference of -18 °C at position 7.

Table 3 Mean, μ, and standard deviation, σ, of temperature differences (simulation – experiment) for the 10 measurement positions shown in Fig. 8.

Position	1	2	3	4	5	6	7	8	9	10
μ (°C)	5.5	0.4	4.7	9.6	7.8	-7.3	-18.0	-7.0	-35.0	-40.1
σ (°C)	8.5	22.9	13.1	8.4	20.3	15.6	22.1	169.8	197.3	137.8

This effect is probably caused by the restriction of the physical effects included in the model. While conduction, convection, and emission are included, the interaction of the deposit walls enclosing positions 6 and 7 or local variation in the surrounding temperature are not considered. Yet, it is noted that for all measurement points on the baseplate the mean difference to the experimental data lies below or very close to the thermal convergence tolerance of 20 K that is applied in the model.

For measurement positions on the deposit (positions 8-10), a more pronounced offset to the experimental data is observed with a widely spread distribution of the temperature differences. While on average, the simulation underestimates the experimental reference, the predicted peak temperatures lie well above the experimentally recorded values. Besides the unknown error introduced by the behavior of the thermocouples under extreme conditions, this issue is closely connected to the discretization of the model.

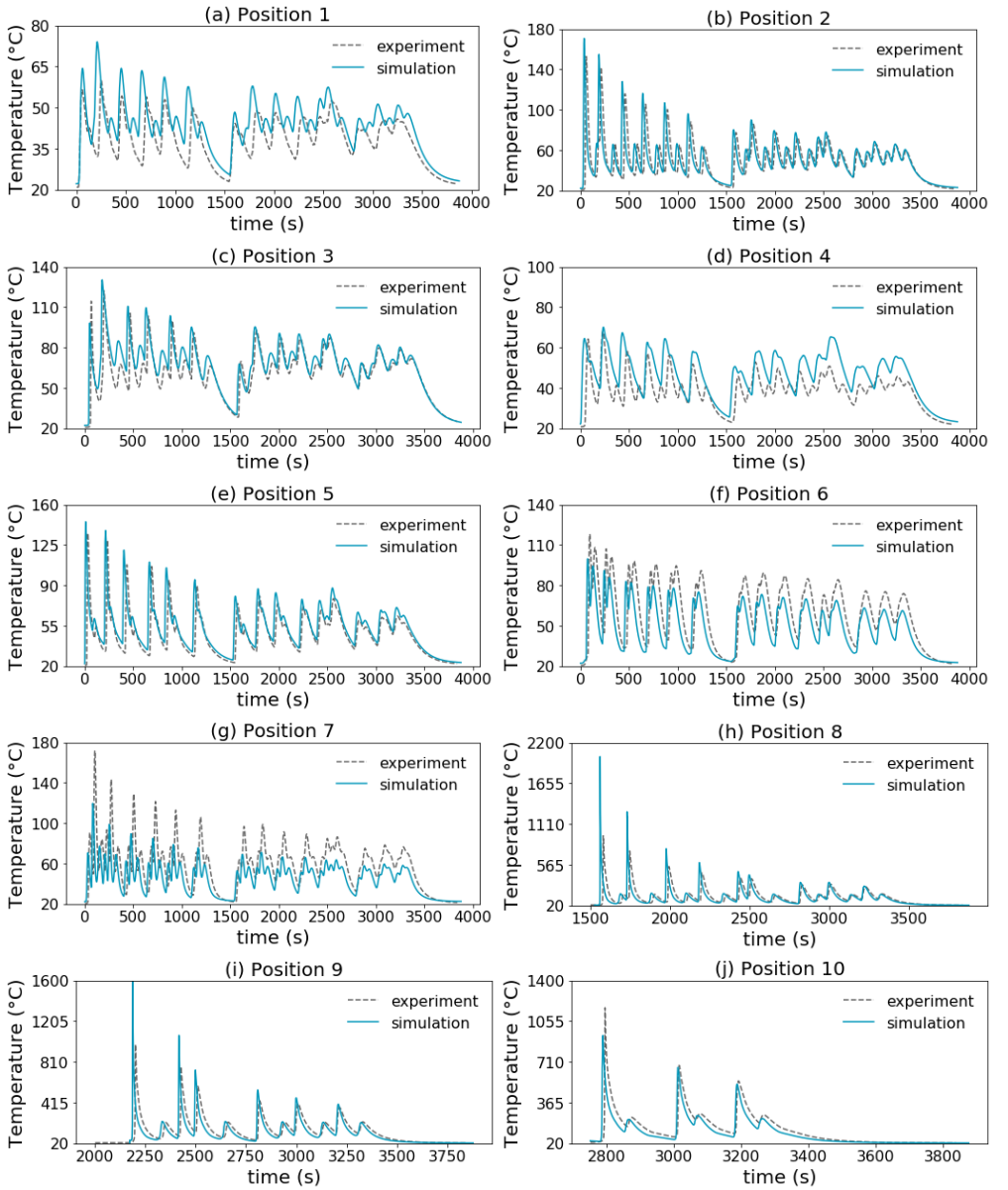

Fig. 9 Experimental and numerical temperature data for the 10 measurement positions shown in Fig. 8

With only one linear element per deposited layer, the temperature difference between the upper and lower edges of the newly deposited element subject to heating has been observed to amount to as much as 800°C. Although this makes it difficult to accurately predict peak temperatures within the model, this localized effect is smoothed out with increasing distance to the weld source.

Despite the scaling of the numerical process time, a slight offset in timing remains between simulation and experiment. In combination with steep temperature gradients, this also contributes to the large standard deviation observed for measurement positions 8 to 10.

Considering the influences discussed above, the numerical analysis reproduces accurately the measured temperature profile, both in the baseplate as well as in the deposit. Thus, the applied model is qualified to serve as a reference for further model simplifications.

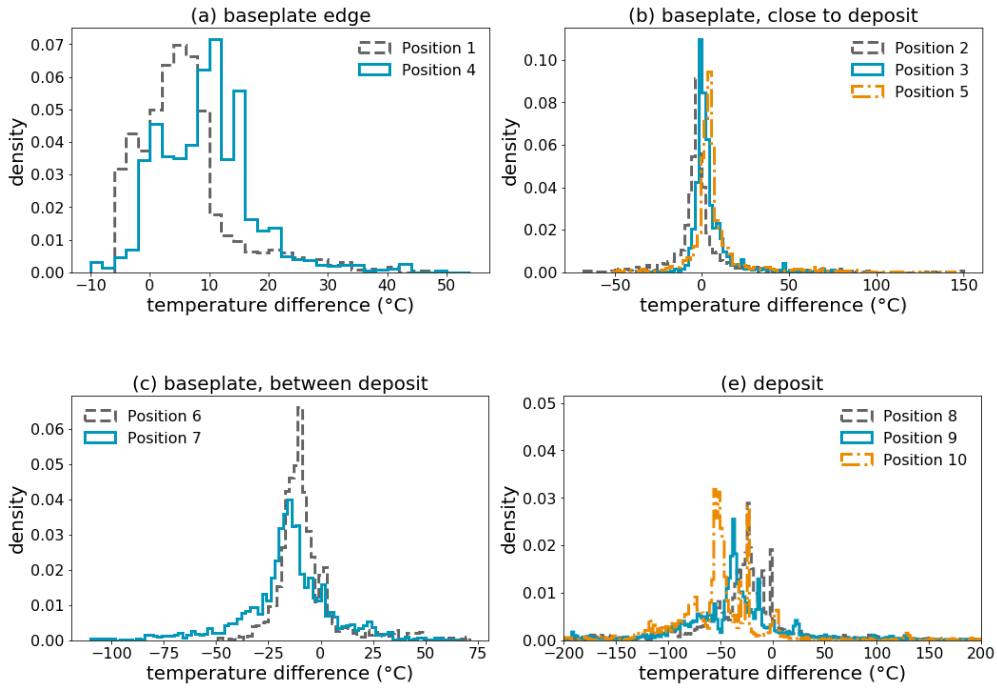

Fig. 10 Distribution of temperature differences (simulation – experiment) for the 10 measurement positions shown in Fig. 8

SIMPLIFIED WELDING MODELS

The performance of the Advanced Thermal Cycle (ATC) described above was tested with reference to the fully transient thermal analysis. Both the influence of the ATC factor as well as the ATC time step were probed. The ATC factor was increased up to the point where entire weld seams are combined into a single segment. This was reached for a value of $N = 688$. For $N = 100$, the bottom layers are split into 15 segments each. In this case, each layer requires a maximum of 30 welding increments to complete while still maintaining a basic representation of the process direction. Fig. 11 exemplarily illustrates the temperature profile for the 6 increments required to complete the second weld bead of the second layer.

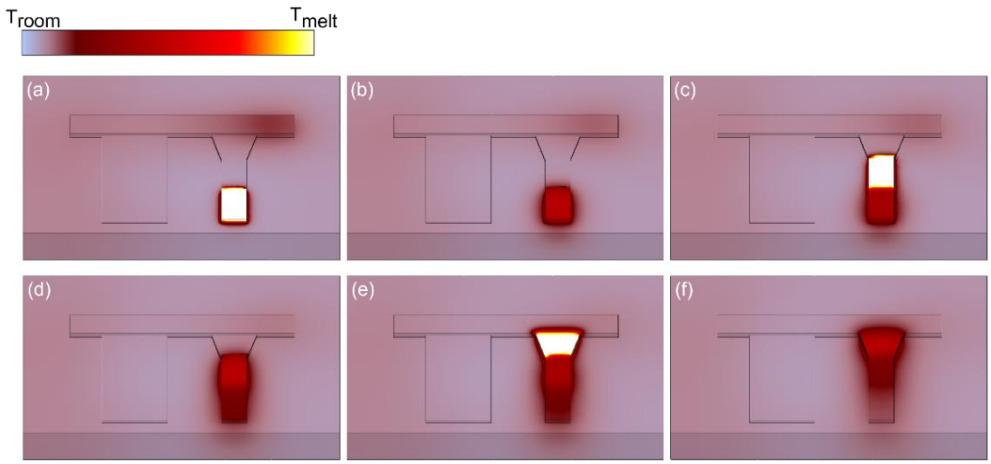

Fig. 11 Temperature profile of the sample while completing the second weld bead of the second layer with ATC factor $N = 100$ and ATC time step $\Theta = 0.8$ *s*.

Table 4 lists the total number of calculated increments for the transient reference and all tested variations of the ATC factor N and ATC time step $\Theta = 0.8$. Table 4, together with the computational times and relative time saving illustrated in Fig. 12, emphasizes the ATC's potential to reduce the computational cost of the simulation. Already with the moderate ATC factor $N = 10$, the time saving with regard to the transient reference amounts to more than 80%. As the ATC factor is increased, the required computational time is further reduced. With increasing ATC factor, the computational time required for the cooling sequences between layers (421 increments for all variants) starts to dominate the total computational time of the simulation. Accordingly, the time saving asymptotically approaches its maximum value that is associated with the ATC combining entire weld beads into one segment each ($N = 688$). In this particular case, the most simplified variant with $N = 688$ could be completed in about 46 minutes, while the variant with $N = 100$ required about 1 hour and 20 minutes.

Table 4 Number of calculated increments for the transient reference and different ATC factors N.

	Transient	***N = 10***	***N = 20***	***N = 50***	***N = 100***	***N = 688***
Nr. of increments	22049	4761	2597	1275	847	509

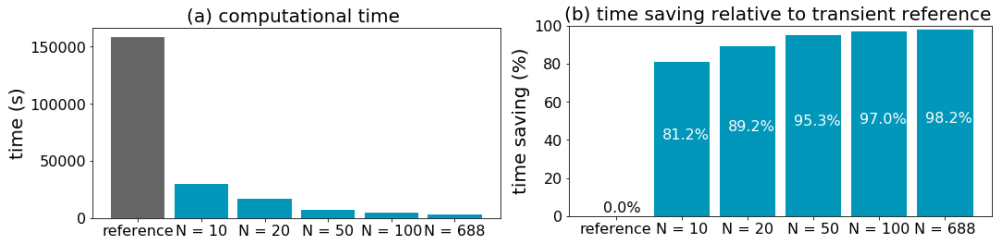

Fig. 12 Computational time and relative time saving for the transient reference and all tested ATC variations with ATC time step $\Theta = 0.8$

With the time saving potential of the ATC established, it is necessary to check how it performs regarding the result quality. Fig. 13 shows exemplarily the thermal profile at positions 6 and 9 recorded for different ATC factors and ATC time step $\Theta = 0.8$. The graphs highlight that the global temperature history is virtually not affected by the simplifications introduced by the ATC with factors up to $N = 100$. Fig. 13 (a) and (c) illustrate that even for $N = 100$, no significant differences are visible when the entire process is considered. Only a close-up of individual temperature peaks (Fig. 13 (b) and (c)) reveals the effect of the ATC and the impact of further simplification with $N = 688$.

Especially the close-up of position 9 (Fig. 13 (d)) illustrates how the time stepping is affected. Depending on the relative positions of the measurement point and the boundaries of the heated segments, the temperature peak is shifted on the time axis or smaller sub-peaks are introduced. Once the heating phase is completed, the heat spreads into the deposit and it is allowed to cool. This part of the curve is much less affected by the localized influence of the weld source and the temperatures measured for the simplified simulations merge again with the transient reference.

Position 6 is not located on the deposit, but on the baseplate. Accordingly, the timing of the temperature peaks is not as much affected by the ATC as for position 9. The close-up of position 6 (Fig. 13 (b)) merely reveals a slight decrease of the recorded peak temperatures as the ATC factor is increased.

Fig. 14 exemplarily illustrates the influence of the ATC time step Θ on the first temperature peaks recorded for constant ATC factor $N = 20$ at positions 8 and 9, respectively. As Θ defines the length of the first increment calculated for each segment, a smaller Θ slightly shifts the temperature peak on the time axis. Due to the shorter time available for heating, a smaller ATC time step leaves less opportunity for heat losses due to conduction, convection, or radiation. Consequently, the peak temperature increases as Θ is decreased as it is observed in Fig. 14. This makes the ATC time step Θ a free parameter that needs to be calibrated to achieve the required peak temperatures. In case of the present model, the best fit was found for $\Theta = 0.8$ s.

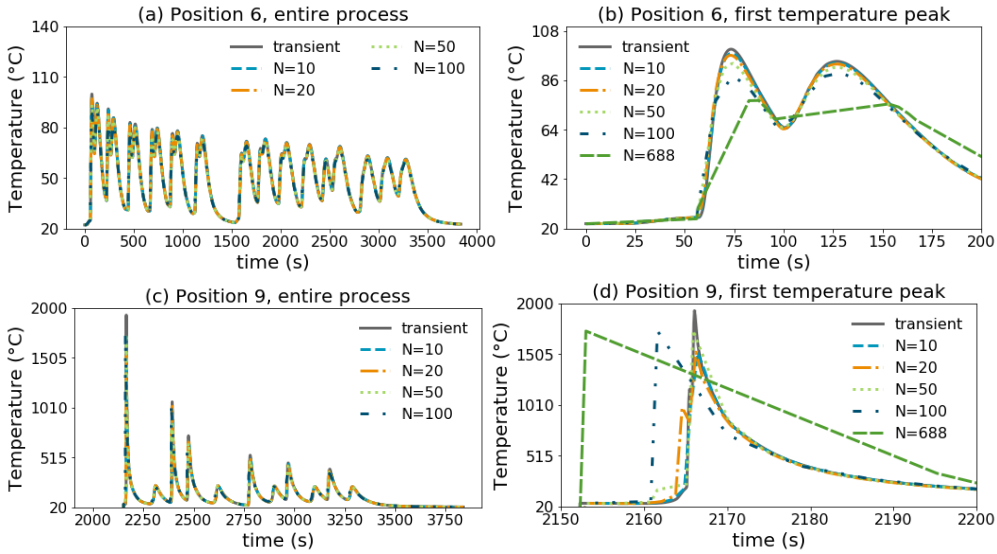

Fig. 13 Temperatures measured at positions 6 and 9 recorded for different ATC factors and ATC time step $\Theta = 0.8$. (a) and (c) show the entire process time, (b) and (d) a close-up of the first temperature peak, respectively

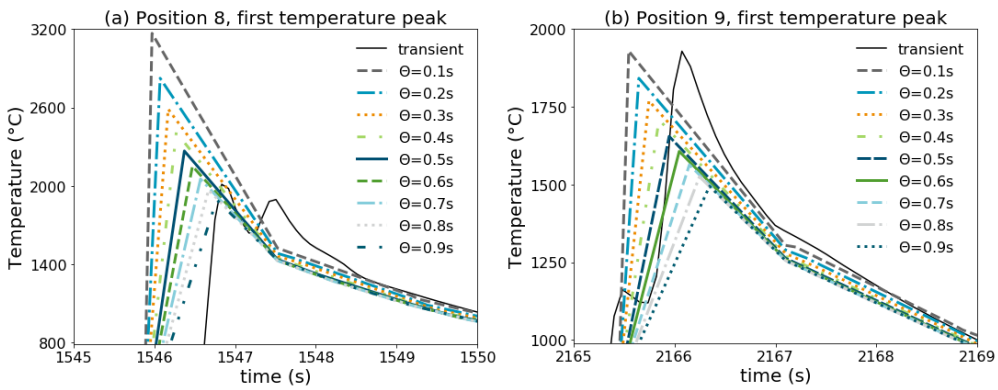

Fig. 14 Variation of the ATC time step Θ for constant ATC factor $N = 20$

CONCLUSIONS

The present contribution shows how a transient DED simulation can be simplified by introducing an Advanced Thermal Cycle (ATC). To test the approach, a transient thermal model was validated by comparison to experimentally measured temperature data recorded both on the baseplate as well as on the deposit itself, and excellent agreement between numerical and experimental data was found. The ATC allows to combine multiple transient time steps into segments for which the heat input is treated in a joint

fashion. It is controlled by two parameters, namely the ATC factor and the ATC time step. The influence of both parameters was evaluated, showing very good agreement between the transient reference and the simplified models. With only a minor loss of result accuracy and resolution in time, the required computational time required for welding could be reduced by more than 97% so that the simulation can be completed within the same time as the real DED built. These results qualify the ATC as a valuable tool for the simulation of large DED processes which cannot be handled via transient simulation otherwise and as a feasible method to evaluate thermal profiles which are difficult to measure experimentally.

References

[1] ASTM INTERNATIONAL: 'ASTM Standard F2792-12a: Standard Terminology for Additive Manufacturing Technologies', 2012, doi: 10.1520/F2792-12A.

[2] P. R. GRADL and C. S. PROTZ: 'Technology advancements for channel wall nozzle manufacturing in liquid rocket engines', *Acta Astronautica*, vol. 174, pp. 148-158, Sep. 2020, doi: 10.1016/j.actaastro.2020.04.067.

[3] B. BLAKEY-MILNER et al.: 'Metal additive manufacturing in aerospace: A review', *Materials & Design*, vol. 209, p. 110008, Nov. 2021, doi: 10.1016/j.matdes.2021.110008.

[4] 'NASA looks to large-scale DED Additive Manufacturing for future rocket engines', *Metal Additive Manufacturing*, Sep. 18, 2020, https://www.metal-am.com/nasa-looks-to-large-scale-ded-additive-manufacturing-for-future-rocket-engines/, accessed Mar. 29, 2022.

[5] S. M. THOMPSON, L. BIAN, N. SHAMSAEI and A. YADOLLAHI: 'An Overview of Direct Laser Deposition for Additive Manufacturing; Part I: Transport Phenomena, Modeling and Diagnostics', *Additive Manufacturing*, vol. 8, p. 36, 2015.

[6] M. BIEGLER, B. A. M. ELSNER, B. GRAF and M. RETHMEIER: 'Geometric distortion-compensation via transient numerical simulation for directed energy deposition additive manufacturing', *Science and Technology of Welding and Joining*, vol. 0, no. 0, pp. 1-8, Mar. 2020, doi: 10.1080/13621718.2020.1743927.

[7] M. BIEGLER, P. KHAZAN, M. GATZEN and M. RETHMEIER: 'Improvement of numerical simulation model setup and calculation time in additive manufacturing-laser-metal-deposition components with an advanced modelling strategy', in *Mathematical Modelling of Weld Phenomena 12*, Seggau, 2018, pp. 979-990. doi: 10.3217/978-3-85125-615-4.

[8] F. MONTEVECCHI, FILIPPO, G. VENTURINI, N. GROSSI and A. SCIPPA: 'Finite Element mesh coarsening for effective distortion prediction in Wire Arc Additive Manufacturing', *Additive Manufacturing*, vol. 18, p. 145, 2017.

[9] E. BOOS et al.: 'Topology Optimized Unit Cells For Laser Powder Bed Fusion', in *Industrial perspectives in Additive Technologies*, pp. 30-39, Vienna, 2021.

[10] G. TURICHIN, E. ZEMLYAKOV, K. BABKIN, S. IVANOV and A. VILDANOV: 'Analysis of distortion during laser metal deposition of large parts', *Procedia CIRP*, vol. 74, pp. 154-157, Jan. 2018, doi: 10.1016/j.procir.2018.08.068.

[11] S. MARIMUTHU et al.: 'Finite element modelling of substrate thermal distortion in direct laser additive manufacture of an aero-engine component', Proceedings of the Institution of Mechanical Engineers, *Part C: Journal of Mechanical Engineering Science*, vol. 227, no. 9, pp. 1987-1999, Sep. 2013, doi: 10.1177/0954406212470363.

[12] V. NAIN, T. ENGEL, M. CARIN, D. BOISSELIER and L. SEGUY: 'Development of an Elongated Ellipsoid Heat Source Model to Reduce Computation Time for Directed Energy Deposition Process', *Frontiers in Materials*, vol. 8, p. 512, 2021, doi: 10.3389/fmats.2021.747389.

[13] Y. YANG, M. ALLEN, T. LONDON and V. OANCEA: 'Residual Strain Predictions for a Powder Bed Fusion Inconel 625 Single Cantilever Part', *Integr Mater Manuf Innov*, vol. 8, no. 3, pp. 294-304, Sep. 2019, doi: 10.1007/s40192-019-00144-5.

[14] Z. BOUMERZOUG, E. RAOUACHE and F. DELAUNOIS: 'Thermal cycle simulation of welding process in low carbon steel', *Materials Science and Engineering: A*, vol. 530, pp. 191-195, Dec. 2011, doi: 10.1016/j.msea.2011.09.073.

[15] T. KIK: 'Computational Techniques in Numerical Simulations of Arc and Laser Welding Processes', *Materials*, vol. 13, no. 3, Art. no. 3, Jan. 2020, doi: 10.3390/ma13030608.